

ENERGY PATTERNS FOR A CONDUCTING CIRCULAR DISC BURIED IN A HOMOGENEOUS LOSSY MEDIUM AND EXCITED BY ULTRA-WIDEBAND GENERALIZED GAUSSIAN PULSES

M. G. M. Hussain and S. F. Mahmoud [†]

Electrical Engineering Department
Kuwait University
P.O. Box 5969, Al-Safat 13060 Kuwait

Abstract—In this paper, we analyze the scattering of ultra-wideband (UWB) electromagnetic pulses from a conducting circular disc, buried in a homogeneous lossy medium. The transient currents excited on the surface of the conducting disc are derived, in the frequency domain, as series expansion of a set of orthogonal functions that satisfy specified boundary conditions. The amplitude spectral density of the surface currents are plotted for a given disc radius, and depth in a lossy medium. A closed form solution for the backscattered electric field strength in the far zone is derived in the frequency domain for the case of a normally-incident plane wave having the time variation of a generalized Gaussian pulse (GGP). The time variation and the energy density spectrum of the GGP signal and that of the backscattered signal in the far zone are plotted too. Computer plots of the backscattered energy versus observation angle, depth, disc radius, altitude from surface of the lossy medium, and the electric properties of the medium, result in various energy patterns that are desirable for the design and performance analysis of UWB ground-penetration impulse radar.

1 Introduction

2 Induced Current Modes

3 Backscattered Electric Field Strength

4 Energy Patterns

[†] Visiting Professor at Queen's University, Kingston, Ontario, Canada

5 Conclusions

References

1. INTRODUCTION

Over-the-past decade, extensive theoretical as well as experimental research has been carried out to develop the applications of the emerging ultra-wideband (UWB) technology. The UWB ground-penetration radar (GPR) has been the main focus of the research efforts in UWB technology, especially for the detection of buried targets such as mines as well as damaged utility pipes [1–5]. A typical problem of interest that is closely related to the area of GPR and the detection of underground mines is the scattering of electromagnetic waves from a conducting disc buried in a homogeneous lossy medium. This problem has been investigated recently in the case of narrow-band sinusoidal waveforms [6, 7]. The main result in [7] is the representation of the excited currents in terms of a complete set of vector eigenfunctions, referred to as current modes, that exhibit mutual orthogonality over the surface of the circular disc. Here, we show that the first current mode is the dominant mode that results in most of the backscattered energy in the far zone.

Experimentation with UWB radiators and sensors has demonstrated that electromagnetic impulses can analytically be represented by a generalized Gaussian pulse (GGP), that is characterized by a frequency spectrum free from a direct-current (dc) component [8, 9]. The mathematical model of the GGP signal is convenient for developing the theory and analysis of UWB technology.

In this paper, we extend the results presented in [7] to analyze the scattering of UWB electromagnetic pulses from a conducting circular disc buried in a lossy medium. The analysis is carried out in the frequency domain.

In Section 2, we present the full-wave general solutions of the induced current modes on the surface of a conducting circular disc buried in a homogenous lossy medium. The excitation electric field strength have the time variation of a GGP signal and it is assumed to be normally incident on the surface of the lossy medium in which the disc is buried. In Section 3, the backscattered electric field strength from the circular disc is derived in the frequency domain for the far zone condition. The frequency spectrum of the far-zone electric field strength is a function of disc radius, depth from the surface, observation (or elevation) angle relative to the disc axis, the far-zone range, and the electric properties of the lossy medium. A plot of the far-zone signal

energy versus any one of these parameters results in an *energy pattern*. In Section 4, Computer plots are presented for the time variation and the energy density spectrum of the incident GGP signal and that of the backscattered signal in the far zone. Also, the time variation and the amplitude density spectrum of the surface-current modes of the buried disc are plotted for the first two significant current modes. Various energy patterns of the backscattered signal are presented too. The energy patterns can be utilized as a design tool for the performance analysis of UWB-impulse GPR.

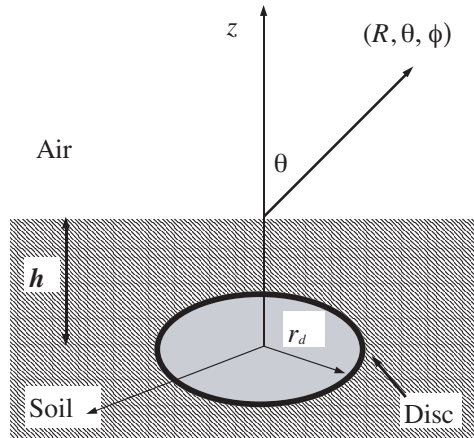


Figure 1. Geometry of a conducting circular disc buried at a depth h in a homogeneous lossy medium.

2. INDUCED CURRENT MODES

A conducting circular disk of radius r_d and negligible thickness is buried at a depth h in a homogeneous lossy medium as shown in Fig. 1. The medium surrounding the disc can be pure soil with permeability μ_0 , which equals that of the free space, and relative complex permittivity ϵ_r . According to the geometry in Fig. 1, the axis of the disc is aligned with the z axis and any point on the surface of the disc has the cylindrical coordinates $(r, \phi, -h)$. A point above the surface of the lossy medium is given by the spherical coordinates (R, θ, ϕ) . The air-medium interface is the plane $z = 0$.

Let a planar wavefront be normally incident, $\theta = 0$, on the plane of the air-medium interface, $z = 0$. The electric field strength of the incident plane wave is assumed to be in the y direction. In this case, the transmitted electric field strength that is incident on the surface of

the disc at $z = -h$ is given in the frequency domain by [7],

$$\begin{aligned}\mathbf{E}(\omega, r, \phi) &= E_0(\omega)T(\omega) \exp\{-\gamma(\omega)h\} \\ &= E_0(\omega)T(\omega) \exp\{-\gamma(\omega)h\} \left(\hat{r} \sin \phi + \hat{\phi} \cos \phi \right).\end{aligned}\quad (1)$$

where $E_0(\omega)$, $\omega = 2\pi f$, f frequency (Hz), is the amplitude spectral density of the incident electric field at the plane $z = 0$. In (1), the transmission coefficient $T(\omega)$ and the propagation coefficient $\gamma(\omega)$ are expressed as follows,

$$T(\omega) = 2/(1 + \varepsilon_r), \quad (2)$$

$$\gamma(\omega) = j\omega\sqrt{\varepsilon_r}/c, \quad (3)$$

where c is the speed of light, and ε_r is the relative complex permittivity of the lossy medium.

The incident electric field $\mathbf{E}(\omega, r, \phi)$ excites the current density $\mathbf{J}(\omega, r, \phi)$ on the surface of the disc. This surface current density can be expressed as a series expansion in terms of two sets of eigen vectors classified as types a , and b modes [7],

$$\mathbf{J}(\omega, r, \phi) = \sum_{p=1}^{\infty} C_p^a(\omega)\mathbf{J}_p^a(r, \phi) + C_p^b(\omega)\mathbf{J}_p^b(r, \phi). \quad (4)$$

The two sets of eigen vectors in (4) are given by the following relationships [7]:

$$\mathbf{J}_p^a(r, \phi) = \hat{r} \frac{J_1(k_p r) \sin \phi}{k_p} + \hat{\phi} J_1'(k_p r) \cos \phi, \quad (5)$$

$$\mathbf{J}_p^b(r, \phi) = \hat{r} J_1'(l_p r) \sin \phi + \hat{\phi} \frac{J_1(l_p r) \cos \phi}{l_p r}, \quad (6)$$

where the $J_1(\cdot)$ is the Bessel function of order 1 and $J_1'(\cdot)$ its derivative with respect to the arguments $k_p r$ and $l_p r$, $p = 1, 2, 3, \dots$

For the circular disc in Fig. 1, the radial component of the surface current density must vanish at the edge where $r = r_d$. According to (5) and (6), this boundary condition can be satisfied by choosing the wave numbers k_p and l_p , $p = 1, 2, 3, \dots, P$, such that for $r = r_d$, the Bessel function $J_1(k_p r_d) = 0$ and its derivative $J_1'(l_p r_d) = 0$.

The current eigen functions in (5) and (6) form a complete set of mutually orthogonal functions. The eigen functions resemble the transverse magnetic fields of TM and TE modes in a circular waveguide with perfect electric walls. The current coefficients $C_p^a(\omega)$ and $C_p^b(\omega)$ (A/m) are unknowns that need to be determined from

boundary conditions. According to (5) and (6), one obtains $\nabla \cdot \mathbf{J}_p^a(r, \phi) = 0$ and $\nabla \times \mathbf{J}_p^b(r, \phi) = 0$. The first condition corresponds to the type *a* set of eigen functions or current modes which are excited on the surface of the disc in the form of closed loops. Hence, the mode *a* surface current density is equivalent to a magnetic multi-pole and produces only TE_z backscattered field. On the other hand, the second condition which corresponds to the type *b* eigen functions is equivalent to an electric dipole and, generally, produces a hybrid backscattered field.

Let us describe the boundary conditions for calculating the current coefficients $C_p^a(\omega)$ and $C_p^b(\omega)$. On the surface of the disc in Fig. 1, the total tangential electric field strength, that is the incident electric field $\mathbf{E}(\omega, r, \phi)$ plus the TE_z backscattered electric field strengths $\mathbf{E}_p^a(\omega, r, \phi)$ and $\mathbf{E}_p^b(\omega, r, \phi)$, equal to the product of the surface current density and the surface impedance of the disc, Z_d ,

$$\begin{aligned} \mathbf{E}(\omega, r, \phi) &+ \sum_{p=1}^{\infty} \left(C_p^a(\omega) \mathbf{E}_p^a(\omega, r, \phi) + C_p^b(\omega) \mathbf{E}_p^b(\omega, r, \phi) \right) \\ &= Z_d \sum_{p=1}^{\infty} \left(C_p^a(\omega) \mathbf{J}_p^a(\omega, r, \phi) + C_p^b(\omega) \mathbf{J}_p^b(\omega, r, \phi) \right). \end{aligned} \quad (7)$$

For a finite set, $p = 1, 2, \dots, P$, of current modes of types *a* and *b*, the boundary condition in (7) yields a set of linear equations that can be solved numerically for the current coefficients $C_p^a(\omega)$ and $C_p^b(\omega)$.

3. BACKSCATTERED ELECTRIC FIELD STRENGTH

The longitudinal backscattered electric and magnetic field strengths in the region $z > 0$, above the surface of the lossy medium, due to the current densities $\mathbf{J}_p^a(\omega, r, \phi)$ and $\mathbf{J}_p^b(\omega, r, \phi)$ are given by the following integrals [7]:

$$E_p^{\{a,b\}}(\omega, z) = \int_0^{\infty} g^2 F_p^{\{a,b\}}(g) T^e(g) \exp(-uh - u_0z) J_1(gr) \sin \phi dg, \quad (8)$$

$$H_p^{\{a,b\}}(\omega, z) = \int_0^{\infty} g^2 G_p^{\{a,b\}}(g) T^h(g) \exp(-uh - u_0z) J_1(gr) \cos \phi dg, \quad (9)$$

where $u = (\gamma^2 + g^2)^{1/2}$, $\gamma = j\omega\sqrt{\mu\epsilon}$, $\gamma_0 = jk_0 = j\omega\sqrt{\mu_0\epsilon_0}$, g is a radial wavenumber, $T^e(g)$ and $T^h(g)$ are the spectral transmission coefficients for TM_z and TE_z , respectively. These two coefficients ensure the continuation of the transverse fields across the air-medium boundary.

In (8) and (9), the superscript $\{a, b\}$ stands for the current modes of type a or type b , and the corresponding functions $F_p^{\{a,b\}}(g)$ and $G_p^{\{a,b\}}(g)$ are given by [7]:

$$F_p^a(g) = 0, \quad (10)$$

$$G_p^a(g) = \frac{-(gr_d/2)}{(g^2 - k_p^2)u} J_1(gr_d) J_1'(k_p r_d), \quad (11)$$

$$F_p^b(g) = \frac{-(l_p r_d/2)}{(g^2 - l_p^2)u} J_1(l_p r_d) J_1'(gr_d), \quad (12)$$

$$G_p^b(g) = \frac{-1}{2g u l_p} J_1(l_p r_d) J_1(gr_d), \quad (13)$$

where $k_p r_d$ is the p^{th} zero of the Bessel function $J_1(x)$, and $l_p r_d$ is the p^{th} zero of the derivative of the Bessel function, $J_1'(x)$. The values $l_1 r_d = 1.84118$ and $l_2 r_d = 5.33144$ are needed for subsequent computations.

The integrals given in (8) and (9) can be evaluated by applying the *stationary phase method of integration* [11]. In the *far-zone* where the conditions $\omega r/c \gg 1$ and $\omega z/c \gg 1$ hold, the stationary point (or phase) of integration for (8) and (9) is given by the relationships $g = g_s = (\omega/c) \sin \theta$ and $u = u_s = j(\omega/c) \cos \theta$. In this case, the solutions for the integrals given in (8) and (9) result in the far-field electric and magnetic field strengths as follows:

$$E_p^b(\omega, R, \theta, \phi) = (\omega/c)^2 F_p^b(\omega, \theta) (1/R) \exp\{-j\omega R/c\} \\ \times T^e(\theta) \exp\{-j(\omega h/c) \sqrt{\varepsilon_r - \sin^2 \theta}\} \sin \theta \cos \theta \sin \phi, \quad (14)$$

$$H_p^{\{a,b\}}(\omega, R, \theta, \phi) = (\omega/c)^2 G_p^{\{a,b\}}(\omega, \theta) (1/R) \exp\{-j\omega R/c\} \\ \times T^h(\theta) \exp\{-j(\omega h/c) \sqrt{\varepsilon_r - \sin^2 \theta}\} \cos \theta \cos \phi. \quad (15)$$

where $F_p^b(\omega, \theta) = F_p^b(g)$, $G_p^{\{a,b\}}(\omega, \theta) = G_p^{\{a,b\}}(g)$, for $g = g_s$, and $u = u_s$, and $R^2 = r^2 + z^2$, $\omega R/c \gg 1$, is the radius of a hemisphere centered at the origin, $r = z = 0$. According to (10), the current modes $\mathbf{J}_p^a(r, \phi)$ result in only TE_z field with the electric field strength $E_p^a(\omega, z) = 0$.

The far-zone components of the electric field strength are given by $E_\theta = -E_p^b(\omega; R, \theta, \phi) / \sin \theta$, and $E_\phi = -\eta_0 H_\theta = \eta_0 H_p^{\{a,b\}}(\omega, R, \theta, \phi) / \sin \theta$; η_0 is the intrinsic impedance of free space.

The spectral transmission coefficients $T^e(\theta)$ and $T^h(\theta)$ are given by:

$$T^e(\theta) = \frac{2\varepsilon_r \sqrt{\varepsilon_r - \sin^2 \theta}}{\sqrt{\varepsilon_r - \sin^2 \theta + \varepsilon_r \cos \theta}}, \quad (16)$$

$$T^h(\theta) = \frac{2\sqrt{\varepsilon_r - \sin^2 \theta}}{\sqrt{\varepsilon_r - \sin^2 \theta + \cos \theta}}, \quad (17)$$

For a total of P current modes generated by the incident field on the surface of the disc in Fig. 1, the θ and the ϕ components of the far-zone electric field strength can be expressed as follows:

$$E_\theta(\omega) = -\sum_{p=1}^P C_p^b(\omega) E_p^b(\omega, R, \theta, \phi) / \sin \theta, \quad (18)$$

$$\begin{aligned} E_\phi(\omega) &= (\eta_0 / \sin \theta) \sum_{p=1}^P C_p^a(\omega) H_p^a(\omega; R, \theta, \phi) \\ &+ \sum_{p=1}^P C_p^b(\omega) H_p^b(\omega, R, \theta, \phi), \end{aligned} \quad (19)$$

The current coefficient $C_p^b(\omega)$ in (18) and (19) can be expressed in terms of the incident electric field strength $E_0(\omega)$ and the propagation characteristics of the lossy medium as follows:

$$C_p^b(\omega) = E_0(\omega) T(\omega) \exp\{-\gamma(\omega)h\} \Upsilon_p^b(\omega). \quad (20)$$

where $\Upsilon_p^b(\omega)$ is regarded as the frequency response of the conducting circular disc in Fig. 1, for the type b current modes. Based on (10) and the boundary condition given by (7), the frequency response of the circular disc $\Upsilon_p^b(\omega)$ can be found numerically for a finite number P of modes from the following relationship,

$$\sum_{p=1}^P \Upsilon_p^b(\omega) \left[Z_d \mathbf{J}_p^b(\omega, r, \phi) - \mathbf{E}_p^b(\omega, r, \phi) \right] = \mathbf{I} \quad (21)$$

where \mathbf{I} is the identity matrix. In Section 4, an UWB pulse is considered as the incident electric field at the surface of the disc in Fig. 1 and computer plots are generated for the time variation and amplitude density spectrums $|C_1^b(\omega)|$ and $|C_2^b(\omega)|$ of the first two current modes. The plots reveal valuable information regarding the significance of only the first current mode producing the backscattered electric field strength (or energy) in the far zone.

4. ENERGY PATTERNS

In Fig. 1, let the normally incident electric field strength at the plane $z = 0$, air-medium boundary, have the time variation of a generalized Gaussian pulse given by [8, 9]

$$\begin{aligned} \Omega(t) = & \frac{E_o}{1-\alpha} \left(\exp\{-4\pi[(t-t_o)/\Delta T]^2\} \right. \\ & \left. - \alpha \exp\{-4\pi[\alpha(t-t_o)/\Delta T]^2\} \right), \alpha \neq 1. \end{aligned} \quad (22)$$

In (22), E_o is the peak amplitude at the time $t = t_o$, ΔT is a nominal duration, and α is a scaling parameter. The function $\Omega(t)$ is referred to as the *generalized Gaussian pulse* (GGP). The time variation of the normalized GGP signal, $\Omega(t)/E_o$, is plotted in Fig. 2a as a function of relative time $t/\Delta T$, for $t_o = 0$, and $\alpha = 0$ (dotted line), 0.75 (dashed line), 1.5 (dashed-dotted line), and 3 (solid line).

The GGP signal has an even symmetry about its peak amplitude at $t = t_o$, and it is characterized by a positive mainlobe and two equal time-sidelobes having purely negative values, which yields the average value $\int_{-\infty}^{+\infty} \Omega(t) dt = 0$. Hence, the GGP is a baseband pulse with no direct-current (dc) component in its energy density spectrum, as we shall demonstrate shortly. According to Fig. 2a, the duration of the mainlobe and the magnitude of the time-sidelobes are decreasing functions of the scaling parameter α . For $\alpha = 0$, the negative time-sidelobes vanish and $\Omega(t)$ becomes an ideal Gaussian pulse as shown in Fig. 2a by the dotted-line. Here, we shall restrict our numerical computations to the value $\alpha = 1.5$.

The Fourier transform of the signal $\Omega(t)$ results in the frequency spectral density function $\Lambda(f)$,

$$\begin{aligned} \Lambda(f) &= \int_{-\infty}^{+\infty} \Omega(t) \exp\{-j2\pi ft\} dt \\ &= \frac{E_o \exp\{-j2\pi t_o(f/\Delta f)\}}{2(1-\alpha)\Delta f} \\ &\times \left(\exp\{-(\pi/4)(f/\Delta f)^2\} - \exp\{-(\pi/4\alpha^2)(f/\Delta f)^2\} \right), \end{aligned} \quad (23)$$

where $\Delta f = 1/\Delta T$ is the nominal frequency bandwidth. The energy spectral density of the GGP signal is given by $\Psi(f) = |\Lambda(f)|^2$ and it is shown in Fig. 2b for $\alpha = 0$ (dotted line), 0.75 (dashed line), 1.5 (dashed-dotted line), and 3 (solid line). The plot for $\alpha = 0$ is the energy density function of an ideal Gaussian pulse and it includes a dc component. The other plots are free from dc component.

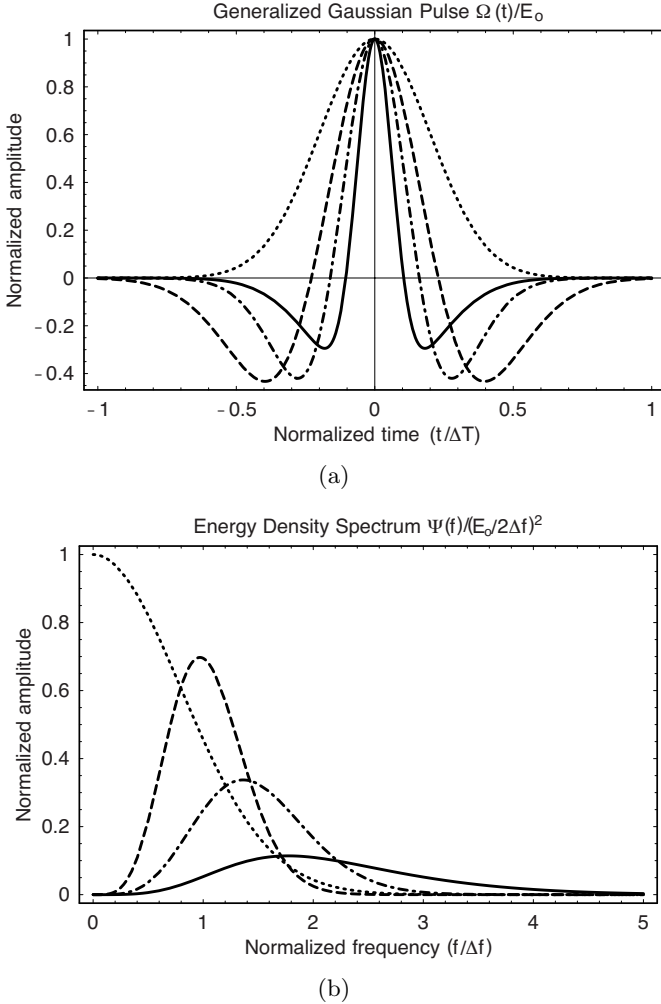
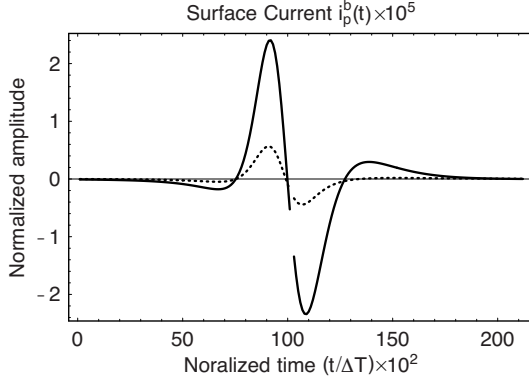


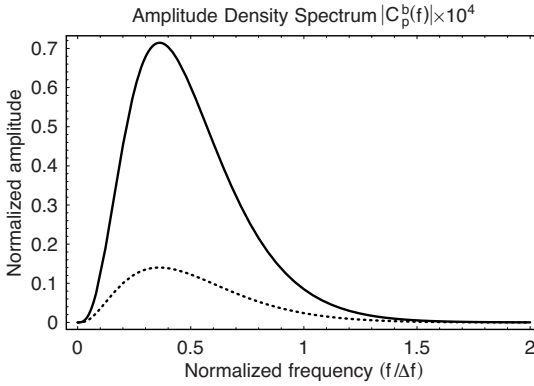
Figure 2. Normalized time variation of the generalized Gaussian pulse $\Omega(t)/E_o$ (a), and energy density spectrum $\Psi(f) = |\Lambda(f)|^2$ (b), for values of the scaling parameter $\alpha = 0$ (dotted line), $\alpha = 0.75$ (dashed line), $\alpha = 1.5$ (dashed-dotted line), and $\alpha = 3$ (solid line).

In the far-zone, the backscattered electric field strength of interest is $E_\theta(\omega)$ given in (18). According to (7) and (10), the electric field strength $E_\theta(\omega)$ is solely due to the current modes of type b given by the relationship in (20).

Computer plots of the time variation of the surface current $i_p^b(t)$



(a)



(b)

Figure 3. Time variation of current mode $i_p^b(t)$ and its amplitude density spectrum $|C_p^b(f)|$ for $p = 1$ (solid line) and $p = 2$ (dotted line). The plots are calculated for normalized disc radius $\rho = 2$, normalized depth $\zeta = 2$, and a homogeneous medium with permittivity $\epsilon_r = 7 - j6$.

and its amplitude density spectrum $|C_p^b(f)|$ are shown in Fig. 3a and Fig. 3b, respectively, for the two significant modes $p = 1$ (solid line), and $p = 2$ (dotted line). The current $i_p^b(t)$ is the inverse Fourier transform of the current spectral density $C_p^b(f)$. The plots in Fig. 3 are numerically calculated using FFT algorithm and with the help of the following substitutions:

$$\rho = r_d \Delta\omega / c, \zeta = h \Delta\omega / c, \xi = R \Delta\omega / c. \quad (24)$$

where ρ is normalized radius of disc, ζ is normalized depth, ξ is

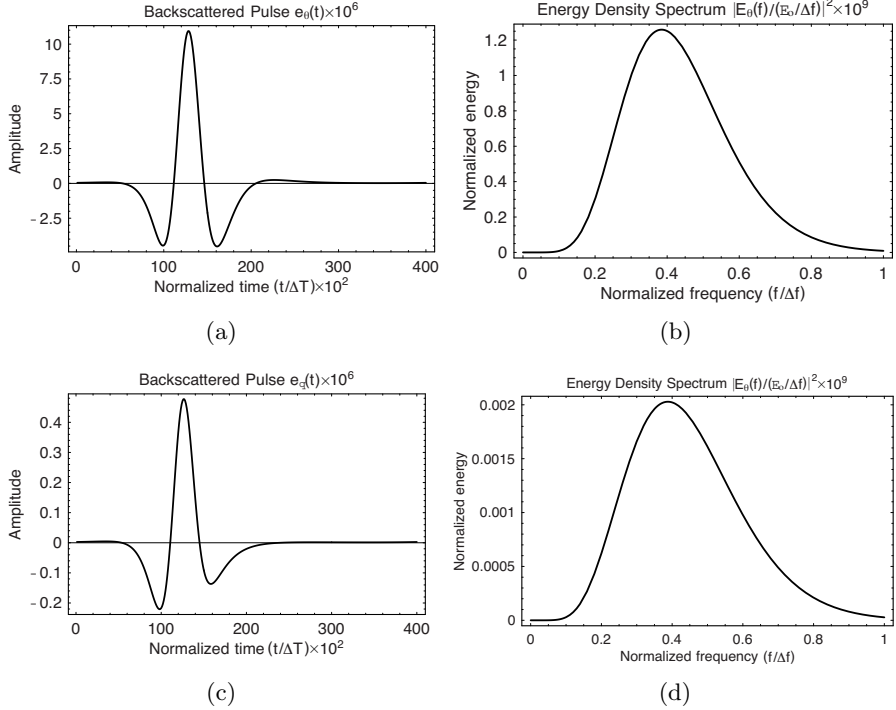


Figure 4. Time variation $e_\theta(t)$ (a), and normalized energy density spectrum $|E_\theta(f)|^2$ (b), of the backscattered electric field strength in the far zone for the mode $p = 1$, and for the mode $p = 2$ in (c) and (d). The plots are calculated for normalized disc radius $\rho = 2$, normalized depth $\zeta = 4$, normalized range $\xi = 20$, and $\varepsilon_r = 7 - j6$.

normalized range, and $\Delta\omega = 2\pi\Delta f$ is nominal bandwidth in (rad/s). The plots in Fig. 3 are calculated for $\rho = \zeta = 2$, and relative complex permittivity $\varepsilon_r = 7 - j6$.

Computer plots of the time variation of the far-zone electric field strength $e_\theta(t)$ and its normalized energy density spectrum $|E_\theta(f)|^2$ are shown in Fig. 4a and Fig. 4b, respectively, for the mode $p = 1$. The same plots are shown in Fig. 4c and Fig. 4d for the mode $p = 2$. The plots in Fig. 4 are calculated for $\rho = \zeta = 2$, $\xi = 20$, and relative complex permittivity $\varepsilon_r = 7 - j6$.

According to Fig. 3, $i_1^b(t)$ is the dominant current mode induced on the surface of the disc in Fig. 1, and Fig. 4 demonstrates that the backscattered electric field strength in the far zone is mainly due to the first mode, $p = 1$. The contributions of the other current modes,

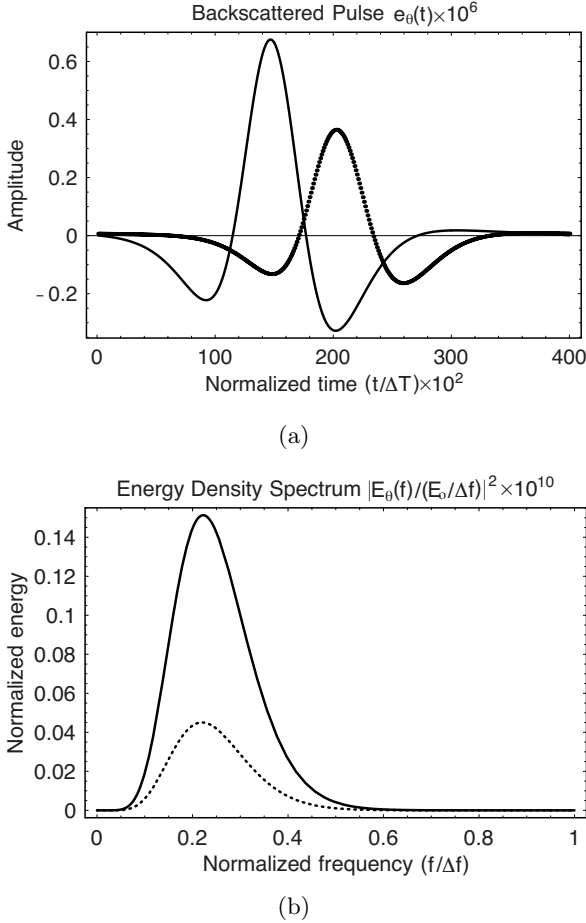


Figure 5. Time variation $e_{\theta}(t)$ (a), and normalized energy density spectrum $|E_{\theta}(f)|^2$ (b) of the backscattered electric field strength in the far zone for normalized disc radius $\rho = 2$, normalized depth $\zeta = 4$, normalized range $\xi = 20$, $\varepsilon_r = 7 - j6$, and observation angles $\theta = 10^\circ$ (solid line), and 50° (dotted line).

$p \geq 2$, and their corresponding electric field strengths in the far zone are negligible.

The time variation of the far-zone electric field strength $e_{\theta}(t)$ and its energy density spectrum $\Gamma(f) = |E_{\theta}(f)|^2$ are shown in Fig. 5a and Fig. 5b, respectively, for the sum of the first two modes $p = 1$ and 2. The plots are for the normalized depth $\zeta = 4$, normalized range $\xi = 20$, normalized disc radius $\rho = 2$, $\varepsilon_r = 7 - j6$, and observation

angle $\theta = 10^\circ$ (solid line), and $\theta = 50^\circ$ (dotted line).

For ground penetration radar, the energy of the backscattered pulse $e_\theta(t)$ is an important parameter for the detection of the buried disc. The backscattered energy is a function of angle θ , disc radius r_d , depth h , range R , nominal bandwidth Δf , and the complex permittivity of the hosting medium ε_r . Hence, the backscattered energy can be expressed in terms of θ, ζ, ρ , and ξ and can be found by the following integrals:

$$W(\theta, \zeta, \rho, \xi) = \int_0^\infty [e_\theta(t)]^2 dt = \int_0^\infty |E_\theta(f)|^2 df. \quad (25)$$

Based on (25), one can derive various *energy patterns* for the circular disc in Fig. 1. The energy patterns are defined by the ratio

$$\frac{W(\theta, \zeta, \rho, \xi)}{W_{max}} = \begin{cases} W(\theta) & \text{for fixed } \zeta, \rho, \xi \\ W(\zeta) & \text{for fixed } \theta, \rho, \xi \\ W(\rho) & \text{for fixed } \theta, \zeta, \xi \\ W(\xi) & \text{for fixed } \theta, \zeta, \rho \end{cases} \quad (26)$$

where W_{max} is the maximum backscattered energy corresponding to each one of the energy patterns given in (26).

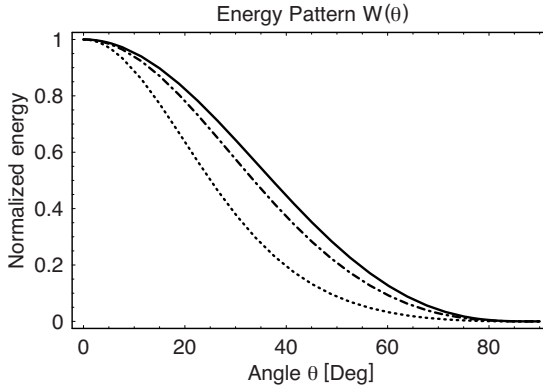


Figure 6. Energy pattern $W(\theta)$ for normalized depth $\zeta = 2$, normalized range in the far zone $\xi = 20$, $\varepsilon_r = 7 - j6$, and normalized radius $\rho = 2$ (solid line), 4 (dashed-dotted line), and 8 (dotted line).

The energy pattern $W(\theta)$ is plotted in Fig. 6 for $\varepsilon_r = 7 - j6$, normalized range $\xi = 20$, normalized depth $\zeta = 2$, and normalized disc radius $\rho = 2$ (solid line), 4 (dashed-dotted line), and 8 (dotted line). The *half-energy beamwidth* of the energy pattern $W(\theta)$ decreases as the value of ρ is increased.

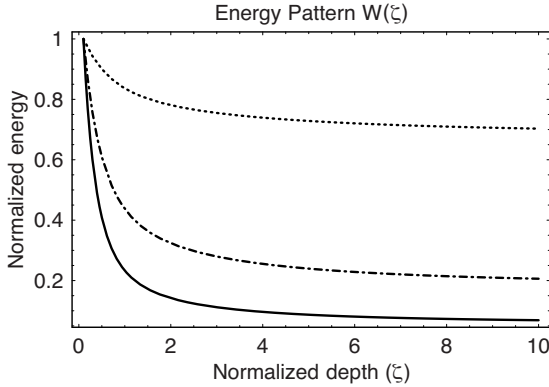


Figure 7. Energy pattern $W(\zeta)$ for observation angle $\theta = 30^\circ$, normalized radius $\rho = 2$, normalized range in the far zone $\xi = 20$, and $\varepsilon_r = 7 - j6$ (solid line), $\varepsilon_r = 7 - j3$ (dashed line), and $\varepsilon_r = 7 - j0.6$ (dotted line).

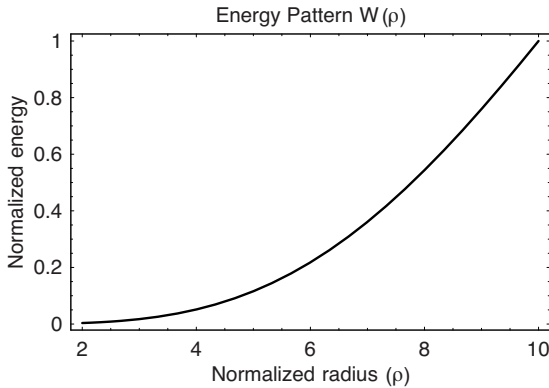


Figure 8. Energy pattern $W(\rho)$ for observation angle $\theta = 30^\circ$, normalized depth $\zeta = 2$, normalized range in the far zone $\xi = 20$, and $\varepsilon_r = 7 - j6$.

The energy pattern $W(\zeta)$ is shown in Fig. 7 for $\theta = 30^\circ$, $\rho = 2$, $\xi = 20$, and $\varepsilon_r = 7 - j6$ (solid line), $\varepsilon_r = 7 - j3$ (dashed-dotted line), and $\varepsilon_r = 7 - j0.6$ (dotted line). The backscattered energy in the far zone is a decreasing function of the normalized depth ζ at which the disc is buried in the lossy medium. This energy pattern also shows that the complex permittivity ε_r of the lossy medium affects the backscattered energy.

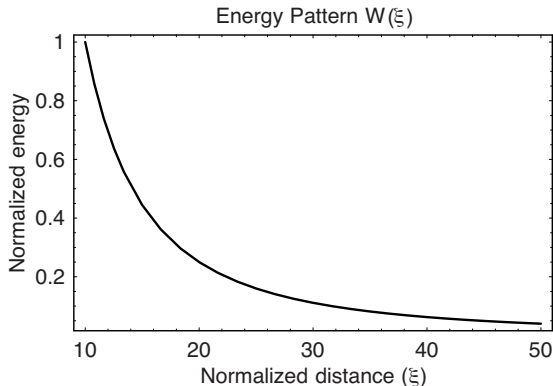


Figure 9. Energy pattern $W(\xi)$ for normalized radius $\rho = 2$, normalized depth $\zeta = 2$, and $\varepsilon_r = 7 - j6$.

The energy pattern $W(\rho)$ is shown in Fig. 8 for $\theta = 30^\circ$, $\zeta = 2$, $\xi = 20$, and $\varepsilon_r = 7 - j6$. The backscattered energy at a fixed point in the far zone is an increasing function of the radius of the buried circular disc in Fig. 1.

The energy pattern $W(\xi)$ is shown in Fig. 9 for $\theta = 30^\circ$, $\rho = \zeta = 2$, and $\varepsilon_r = 7 - j6$. The plot shows that the backscattered energy is a decreasing function of normalized range; $W(\xi) \propto 1/\xi^2$.

The energy patterns in Fig. 6 through Fig. 9 are of interest for the design and performance analysis of UWB ground penetration radar emitting electromagnetic pulses that can analytically be represented by the GGP signal $\Omega(t)$ given in (22).

5. CONCLUSIONS

The scattering of UWB electromagnetic GGP signals from a conducting circular disc buried in a homogeneous lossy medium is analyzed. General solutions for the induced current modes on the surface of the buried disc are presented and plotted for the first two significant modes. Also, solution for the backscattered electric field strength is derived under the far-zone condition, and the assumption of a normally incident planar wavefront with the time variation of a GGP signal. The time variation and the energy density spectrum of the backscattered signal in the far zone are plotted for different observation angles. Various energy patterns for the backscattered signal are presented too. The energy patterns are valuable for the performance analysis of UWB-impulse GPR.

REFERENCES

1. Vitebskiy, S. and L. Carin, "Moment method modeling of short pulse scattering from and the resonances of a wire buried inside a lossy, dispersive half space," *IEEE Trans. On Antennas and Propagation*, Vol. 43, No. 11, 1303–1312, November 1995.
2. Vitebskiy, S. and L. Carin, "Resonances of perfectly conducting wires and bodies of revolution buried in a lossy dispersive half space," *IEEE Trans. On Antennas and Propagation*, Vol. 44, No. 12, 1575–1583, December 1996.
3. Vtebskiy, S., L. Carin, M. Ressler, and F. Lee, "Ultra-widenand, short pulse ground penetrating radar: Theory and measurement," *IEEE Trans. On Geosci. Remote Sensing*, Vol. 35, 762–772, May 1997.
4. Geng, N. and L. Carin, "Wide band electromagnetic scattering from a dielectric BOR buried in a layered lossy dispersive medium," *IEEE Trans. On Antennas and Propagation*, Vol. 47, No. 4, 610–619, April 1999.
5. Carin, L., N. Geng, M. Mclure, J. Sichina, and L. Nyuyen, "Ultra-wide band synthetic-aperture radar for mine-field detection," *IEEE AP Magazine*, Vol. 41, No. 1, 18–33, Feb. 1999.
6. Mahmoud, S. F., "Full wave analysis scattering of electromagnetic waves from a buried conducting disc," *Record International Symposium on Electromagnetic Theory*, Victoria, Canada, May 13–17, 2001.
7. Mahmoud, S. F., "Full wave analysis of electromagnetic wave scattering from an imperfectly conducting circular disc," *J. of Electromagnetic Waves and Applications (JEMWA)*, Vol. 15, No. 7, 917–932, 2001.
8. Hussain, M. G. M., "Principles of space-time array processing for ultrawide-band impulse radar and radio communications," *IEEE Trans. Vehicula Technology*, Vol. 51, No. 3, 393–403.
9. Hussain, M. G. M., "Signal design for ultra-wideband radar and wireless communications," *Proc. 3rd WSES Symposium on Mathematical Methods and Computational Techniques in Electrical Engineering 2001*, Athens, Greece, Dec. 2001.
10. Wait, J. R., *Geo-Electromagnetism*, Academic Press, New York, 1982.
11. Clemmow, P. C., *The Plane Wave Representation of Electromagnetic Fields*, Pergamon Press, New York, 1966.